A fast and robust numerical scheme for solving models of charge carrier transport and ion vacancy motion in perovskite solar cells

N. E. Courtier[a,*], G. Richardson[a], J. M. Foster[b]

[a] *Mathematical Sciences, University of Southampton, SO17 1BJ, UK*
[b] *Department of Mathematics, University of Portsmouth, Portsmouth, PO1 2UP, UK*

Abstract

Drift-diffusion models that account for the motion of ion vacancies and electronic charge carriers are important tools for explaining the behaviour, and guiding the development, of metal halide perovskite solar cells. Computing numerical solutions to such models in realistic parameter regimes, where the short Debye lengths give rise to boundary layers in which the solution varies extremely rapidly, is challenging. Two suitable numerical methods, that can effectively cope with the spatial *stiffness* inherent to such problems, are presented and contrasted (a finite element scheme and a finite difference scheme). Both schemes are based on an appropriate choice of non-uniform spatial grid that allows the solution to be computed accurately in the boundary layers. An adaptive time step is employed in order to combat a second source of stiffness, due to the disparity in timescales between the motion of the ion vacancies and electronic charge carriers. It is found that the finite element scheme provides significantly higher accuracy, in a given compute time, than both the finite difference scheme and some previously used alternatives (Chebfun and `pdepe`). An example transient sweep of a current-voltage curve for realistic parameter values can be computed using this finite element scheme in only a few seconds on a standard desktop computer.

Keywords: Perovskite solar cell; ion vacancy; drift-diffusion; finite element; finite difference; stiffness.

1. Introduction

Recent rapid improvements in power conversion efficiency have brought metal halide perovskite solar cells (PSCs) to the forefront of the emerging thin-film photovoltaic technologies. Efficiencies in excess of 20% [1, 2], which are comparable to those of standard crystalline silicon devices, have been achieved using perovskite materials as absorber layers in thin film architectures. This high performance, together with their relatively low cost of manufacture, mean that the continued development of PSCs is an extremely active area of research.

*Corresponding author
Email address: `nc4g14@soton.ac.uk` (N. E. Courtier)

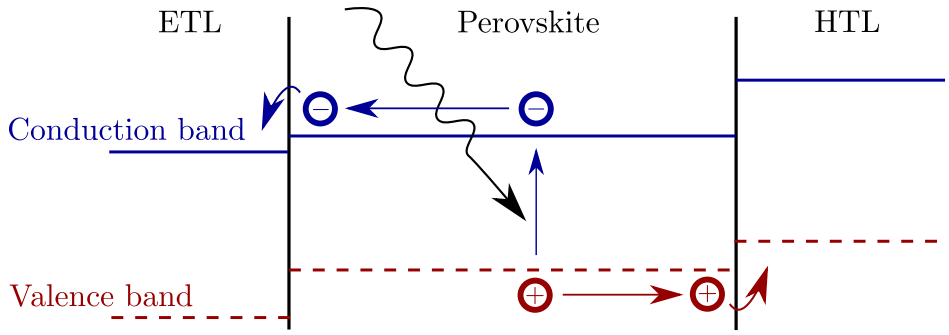

Figure 1: Sketch of a planar PSC showing the structure of the conduction (blue solid lines) and valence (red dashed lines) bands and the flow of electrons and holes.

Current research aims not only to further improve their efficiency but also to extend device lifetimes. Reviews of the field have been given in [3, 4, 5, 6, 7].

Planar PSC architectures are formed by a perovskite absorber layer sandwiched between an electron transport layer (ETL) and a hole transport layer (HTL), see figure 1. The most commonly used perovskite absorbing material is methylammonium lead tri-iodide ($CH_3NH_3PbI_3$) [8], however, recently other mixed halide formulations (in which some of the iodide ions are substituted by other halides) and mixed cation formulations (in which the methylammonium cation is fully or partially replaced with *e.g.* formamidinium and/or cesium) have also been successfully employed [9, 10, 2]. Numerous different materials have been used as ETLs and HTLs but common choices are titania (TiO_2) for the former and spiro-MeOTAD for the latter.

Under illumination, incident photons with energies above the band gap are absorbed in the perovskite layer generating weakly bound excitons (binding energy ∼50 meV [11]). These excitons readily dissociate into a free electron in the conduction band and a hole in the valence band which then move under the influences of both thermally-induced diffusion and electronically-induced drift. The transport layer materials are chosen such that the conduction band in the HTL is above that in the perovskite and the valence band in the ETL is below that in the perovskite, resulting in energy barriers that prevent the entry of holes into the ETL and electrons into the HTL. The differences in the band energies of the different semiconductors also lead to the formation of a built-in field in the perovskite which drives electrons towards the ETL and holes towards the HTL. A cartoon of this process is shown in figure 1.

One notable peculiarity of PSCs is their long timescale transient behaviour occurring on the order of tens of seconds. This is observed both in current transients [12, 13] and in current-voltage (J-V) curves, a phenomenon which has been termed *hysteresis* by the field [14, 13]. Initially, three possible explanations for the slow (relative to charge carrier motion) dynamics were postulated [14], namely: (i) the formation of ferroelectric domains (ii) large-scale trapping of electrons, and (iii) mobile ions. However, there is a growing consensus that the only mechanism that offers a coherent explanation of the experimental data is the slow motion of positively charged anion vacancies [1, 15]. More recently, very long timescale

reversible transients in the efficiency of PSCs have been observed over periods of several hours, which have been attributed to the motion of cation vacancies [16].

A range of approaches exist to modelling PSC behaviour that extend from fundamental atomistic density functional theory (DFT) calculations (*e.g.* [17]) to equivalent circuit device models (*e.g.* [18]). High computational costs mean that DFT can only be applied to a few atoms and over extremely short timescales. At the other extreme, equivalent circuit models, which are very straightforward to solve, are hard to connect directly to the device physics. An intermediate path, which leads to a computationally tractable model that can be directly interpreted in terms of device physics, is given by charge transport, or equivalently drift-diffusion, modelling. Notably this approach allows for parameters obtained from DFT calculations on the perovskite structure to be incorporated into the model [15]. It has also been used in a variety of other solar cell applications, for example in organics [19, 20, 21].

Initially the importance of ion motion in PSCs was not fully appreciated and as a consequence charge transport models that treated only electron and hole transport were formulated [22, 23]. Subsequently models incorporating ion motion were investigated. The additional physics in these revised models has necessitated that new methods for their solution have been developed. Numerical approaches were taken in [24, 25, 26, 27] while combined asymptotic/numeric methods were used by [15, 12, 16, 28]. To date, numerical approaches have only been able to obtain solutions to models that have been simplified. The solution methods in [24, 27] rely on decoupling the relatively slow ion motion from the charge carrier transport. Ion motion is also decoupled from that of the carriers in [26], in which ion accumulation is incorporated in the form of narrow layers of uniform charge adjacent to each interface within the perovskite. In [25], approximations are made to the physical system that is being modelled, including constant band energies across the three different semiconductors and diffuse interface regions ($\sim$10 nm wide) across which interface recombination is applied. Approximations have been used because the incorporation of realistic densities of ion vacancies (as high as 10^{19} cm^{-3} [29]) leads to a model that is computationally challenging to solve owing to (i) narrow Debye layers across which rapid changes in solution occur, (ii) very large changes in the magnitude of the solution across the device and (iii) the large disparity between the timescales for ion vacancy motion and electron and hole transport. Of the aforementioned works on charge transport modelling of PSCs, only [12, 15, 28] manage to obtain solutions in physically relevant parameter regimes. In these studies, the analysis relies on asymptotic approximations, including the assumption that the carrier densities remain much smaller than the ion vacancy density during the relevant experimental procedure. Whilst these approximations are well-justified in most scenarios, and lead to accurate approximate solutions, a numerical treatment of the full system of equations, that is capable of furnishing solutions across all relevant timescales and operating regimes without simplification, is highly desirable. Motivated by the absence of such a method in the literature, the aim of this work is to present a numerical scheme capable of obtaining accurate solutions to a fully coupled charge transport model of a PSC.

The work is set out as follows. In the next section, we outline the charge transport model, non-dimensionalise and give estimates for the sizes of the dimensionless parameters. In §3,

we describe the spatial discretisation and implementation of our finite element scheme in MATLAB [30]. Then in §4, the equivalent description is given for our finite difference scheme whose implementation (also in MATLAB) uses the Advanpix Multi-Precision Toolbox [31]. Results obtained using this scheme were previously used for verification of our asymptotic method [28]. In §5, we demonstrate the pointwise convergence of the two methods and the importance of the spatial grid on both accuracy and computation time. We also benchmark the two schemes against MATLAB's built-in solver `pdepe`, previously used on a uniform grid [25]. We also briefly discuss how the various approaches compare to our attempts to use spectral methods [15]. In §6, we compare solutions obtained using the finite element scheme and the asymptotic approach developed in [28, 32] for some experimentally motivated test cases. Finally, in §7, we present our conclusions.

2. The charge transport model

We consider a model for a planar PSC consisting of a perovskite absorber layer sandwiched between highly doped electron and hole transport layers. As in [15], we assume the doping, and the resulting high conductivity of the transport layers, allows us to treat these layers as 'quasi-metals' through which the electric potential is uniform and equal to that on their respective contacts. In turn this leads to a *single-layer model* in which all the relevant physics takes place within the perovskite layer. Notably, the numerical scheme that we develop for the single-layer model can easily be extended to more realistic multi-layer models. For example, a three-layer model that incorporates charge carrier dynamics in the electron and hole transport layers. An investigation of this three-layer model will be the subject of future work.

2.1. The single layer model equations

The key variables in the problem are time, t; the perpendicular distance from the interface of the perovskite layer with the ETL, x; the mobile anion vacancy density, P; the free-electron density, n; the hole density, p; the electric field (in the x-direction), E; the electric potential, ϕ; the anion vacancy flux (in the x-direction), F^P; and the electron and hole current densities, j^n and j^p, respectively. The key physical processes are the motion, generation and recombination of mobile charge carriers (electrons and holes) and their interaction with the much less mobile anion vacancies and a uniformly distributed stationary cation vacancy distribution. In a perovskite layer of width b, the conservation of holes and free-electrons is described by

$$\frac{\partial p}{\partial t} + \frac{1}{q}\frac{\partial j^p}{\partial x} = G(x) - R(n,p), \quad \text{where} \quad j^p = -qD_p\left(\frac{\partial p}{\partial x} + \frac{p}{V_T}\frac{\partial \phi}{\partial x}\right), \tag{1}$$

$$\frac{\partial n}{\partial t} - \frac{1}{q}\frac{\partial j^n}{\partial x} = G(x) - R(n,p), \quad \text{where} \quad j^n = qD_n\left(\frac{\partial n}{\partial x} - \frac{n}{V_T}\frac{\partial \phi}{\partial x}\right), \tag{2}$$

where q the elementary charge, $G(x)$ is the photo-generation rate; $R(n,p)$ is the bulk recombination and thermal generation rate (henceforth abbreviated to recombination rate); D_p

and D_n are the hole and free-electron diffusivities, respectively; and, V_T the thermal voltage (*i.e.* k_BT/q where T the absolute temperature). The conservation of positively-charged anion vacancies takes the form

$$\frac{\partial P}{\partial t} + \frac{\partial F^P}{\partial x} = 0, \quad \text{where} \quad F^P = -D_+ \left(\frac{\partial P}{\partial x} + \frac{P}{V_T} \frac{\partial \phi}{\partial x} \right), \tag{3}$$

where D_+ is the anion vacancy diffusion coefficient. These conservation equations couple to Poisson's equation:

$$\frac{\partial E}{\partial x} = \frac{q}{\varepsilon} \left(P - N_0 + p - n \right), \quad \text{where} \quad E = -\frac{\partial \phi}{\partial x}, \tag{4}$$

in which N_0 is the uniform density of cation vacancies (and, in order that the material obeys global charge neutrality, is also the average anion vacancy density) and ε is the permittivity of the perovskite.

2.2. Boundary and initial conditions

At the interfaces with the ETL (on $x = 0$) and the HTL (on $x = b$) we require that there is no flux of anion vacancies and that the potential is specified (and equal to that in the adjacent contact). In addition, n_b, the free electron concentration on $x = 0$, is determined by the band energy offsets with the ETL; p_b, the hole concentration on $x = b$, is determined by the band energy offsets with the HTL; and, $j_p|_{x=0}$ and $j_n|_{x=b}$ are determined by R_l and R_r, the rates of surface recombination on these interfaces. Hence, the boundary conditions read

$$F^P|_{x=0} = 0, \quad \phi|_{x=0} = \frac{V_{bi} - V_{ap}}{2}, \quad n|_{x=0} = n_b, \quad j_p|_{x=0} = -qR_l(p), \tag{5}$$

$$F^P|_{x=b} = 0, \quad \phi|_{x=b} = -\frac{V_{bi} - V_{ap}}{2}, \quad p|_{x=b} = p_b, \quad j_n|_{x=b} = -qR_r(n), \tag{6}$$

where V_{ap} is the applied voltage and V_{bi} is the built-in potential. The problem is closed by initial conditions for the electron, hole and anion vacancy concentrations which we denote:

$$n|_{t=0} = n_{\text{init}}(x), \quad p|_{t=0} = p_{\text{init}}(x), \quad P|_{t=0} = P_{\text{init}}(x). \tag{7}$$

2.3. Non-dimensionalisation

In order to identify the origins of the numerical *stiffness* of the problem, we non-dimensionalise the problem as follows.

$$\begin{aligned}
&x = bx^*, && t = \tau_{ion} t^*, && p = \Pi_0 p^*, && n = \Pi_0 n^*, \\
&j^p = qF_{ph} j^{p*}, && j^n = qF_{ph} j^{n*} && P = N_0 P^*, && F^P = \frac{D_+ N_0}{b} F^{P*}, \\
&\phi = V_T \phi^*, && E = \frac{V_T}{b} E^*, && V_{ap} = V_T \Phi^*, && V_{bi} = V_T \Phi^*_{bi}, \\
&G = \frac{F_{ph}}{b} G^*, && R = \frac{F_{ph}}{b} R^*, && R_l = F_{ph} R^*_l, && R_r = F_{ph} R^*_r.
\end{aligned} \tag{8}$$

Here, F_{ph} is the incident photon flux and we take Π_0 to be the characteristic carrier density required to remove the photo-generated charge in the absence of an electric field and τ_{ion} to be the characteristic timescale for ion motion, defined by

$$\Pi_0 = \frac{F_{ph} b}{\hat{D}}, \qquad \tau_{ion} = \frac{L_d b}{D_+}, \qquad \text{and} \qquad L_d = \left(\frac{\varepsilon V_T}{q N_0}\right)^{1/2}, \tag{9}$$

where $\hat{D}$ is a typical carrier diffusivity and L_d is the Debye length calculated based on the most populous charged species, which in this instance is the ion vacancies. The non-dimensionalisation gives rise to the following dimensionless quantities that characterise the system

$$\begin{aligned} &\nu = \frac{D_+ b}{\hat{D} L_d}, && \kappa_p = \frac{D_p}{\hat{D}}, && \kappa_n = \frac{D_n}{\hat{D}}, && \lambda = \frac{L_d}{b}, \\ &\delta = \frac{\Pi_0}{N_0}, && \bar{n} = \frac{n_b}{\Pi_0}, && \bar{p} = \frac{p_b}{\Pi_0}, && \Phi_{bi} = \frac{V_{bi}}{V_T}. \end{aligned} \tag{10}$$

The interpretation of these parameters is self-evident from their definition except perhaps for ν, which is a ratio of the timescales for electronic and ionic motion.

2.4. The non-dimensional model

On dropping the star notation, the dimensionless model consists of the three conservation equations

$$\frac{\partial P}{\partial t} + \lambda \frac{\partial F^P}{\partial x} = 0, \quad \text{where} \quad F^P = -\left(\frac{\partial P}{\partial x} - PE\right), \tag{11}$$

$$\nu \frac{\partial n}{\partial t} = \frac{\partial j^n}{\partial x} + G(x) - R(n,p), \quad \text{where} \quad j^n = \kappa_n \left(\frac{\partial n}{\partial x} + nE\right), \tag{12}$$

$$\nu \frac{\partial p}{\partial t} = -\frac{\partial j^p}{\partial x} + G(x) - R(n,p), \quad \text{where} \quad j^p = -\kappa_p \left(\frac{\partial p}{\partial x} - pE\right), \tag{13}$$

in which $G(x)$ and $R(n,p)$ represent rates of charge carrier generation and recombination, respectively, coupled to Poisson's equation

$$\frac{\partial E}{\partial x} = \frac{1}{\lambda^2}\left(P - 1 + \delta\left(p - n\right)\right), \quad \text{where} \quad E = -\frac{\partial \phi}{\partial x}. \tag{14}$$

The term $(P - 1 + \delta\,(p - n))$, in the equation above, is the dimensionless charge density and comprises contributions from anion vacancies, stationary cation vacancies, holes and electrons, respectively. In practice, the three dimensionless parameters λ (the ratio of the Debye length L_d to the the perovskite layer width), ν (the ratio of the timescales for charge carrier motion to that for ion vacancy motion) and δ (the ratio of typical carrier concentration to typical vacancy concentration) are all very small, see (18).

Equations (11)-(14) hold within the perovskite layer which is bounded by its interface with the ETL, on $x = 0$, and its interface with the HTL, on $x = 1$. The non-dimensional boundary and initial conditions are

$$F^P|_{x=0} = 0, \quad \phi|_{x=0} = \frac{\Phi_{bi} - \Phi(t)}{2}, \quad n|_{x=0} = \bar{n}, \quad j_p|_{x=0} = -R_l(p), \tag{15}$$

$$F^P|_{x=1} = 0, \quad \phi|_{x=1} = -\frac{\Phi_{bi} - \Phi(t)}{2}, \quad p|_{x=1} = \bar{p}, \quad j_n|_{x=1} = -R_r(n), \tag{16}$$

$$P|_{t=0} = P_{\text{init}}(x), \quad n|_{t=0} = n_{\text{init}}(x), \quad p|_{t=0} = p_{\text{init}}(x). \tag{17}$$

Here the total potential drop across the cell, $\phi|_{x=0} - \phi|_{x=1} = \Phi_{bi} - \Phi(t)$, is split into two parts; a built-in potential difference, Φ_{bi}, that arises from the difference in band energies between the ETL and the HTL and an applied potential difference, $\Phi(t)$. Under the scalings used here, see (8), potentials are measured in units of the thermal voltage which is approximately 0.026V. The dimensional built-in voltage is typically around 1.1V and standard experiments vary the dimensional applied voltage within the range of -0.5 to 2V, therefore the total dimensionless potential drop across the cell, $\Phi_{bi} - \Phi(t)$, (measured in units of $V_T \approx 0.026$V) can be quite large. In turn this leads to very large variations in both ion vacancy and carrier concentrations across the perovskite layer and makes the numerical solution of the problem challenging.

2.5. Dimensionless parameter estimates

In Section 2 of [28], an analogous model and non-dimensionalisation are presented for the case where the cation vacancies, as well as the anion vacancies, are mobile. It is shown that, for a typical planar device formed by a 600 nm thick, methylammonium lead tri-iodide perovskite absorber layer sandwiched between a titania ETL layer and a spiro HTL layer, the dimensionless parameters defined in (10) take the values

$$\begin{aligned} &\nu \approx 5.8 \times 10^{-10}, \quad \kappa_p \approx 1, \quad \kappa_n \approx 1, \quad \lambda \approx 2.4 \times 10^{-3}, \\ &\delta \approx 2.1 \times 10^{-7}, \quad \bar{n} \approx 20, \quad \bar{p} \approx 0.30, \qquad \Phi_{bi} \approx 40. \end{aligned} \tag{18}$$

The difficulty in solving (11)-(17) arises from the extreme values of the parameters ν, λ and $\Phi_{bi} - \Phi(t)$. The very small value of ν reflects the large disparity in timescales for the electronic (fast) and ionic (slow) motion. This feature of the problem necessitates the use of an adaptive timestep since any fixed time stepping method would either be prohibitively slow or incapable of capturing the fast electronic dynamics. As is typical for many electrochemical problems (see *e.g.* [33]), the parameter characterising the ratio of the Debye length to the domain length, in this case λ, is also extremely small. This gives rise to appreciable stiffness in the system owing to the rapid changes in the solution across the narrow Debye layers. This issue is further exacerbated by the relatively large value of $\Phi_{bi} - \Phi(t)$. The concentrations of the different charge species in the narrow Debye layers are approximately Boltzmann distributed, *i.e.* they vary exponentially with the potential. A typical change in dimensional potential across one of the two Debye layers of 0.5V corresponds to a dimensionless potential

drop of around 20. This estimate results in a change in n, p or P by a factor of around $\exp(20) \approx O(10^9)$ across a region of dimensionless width $O(10^{-3})$. Therefore, what at first glance appears to be merely a stiff problem is actually an extremely stiff problem. Notably, depending on the approach to spatial discretisation, these very large changes in the magnitudes of the concentrations of the charged species can give rise to large condition numbers in the discrete counterparts of the partial differential equations (PDEs) leading to significant round off errors.

3. Finite element scheme

The central technique underlying both numerical schemes presented in this work is the method of lines. Since the equation governing the electric potential is elliptic, in contrast to those for the charge carrier densities which are parabolic, the discrete system takes the form of a system of coupled differential-algebraic equations (DAEs). As such, it requires a specialised algorithm for temporal integration. Here, we employ MATLAB's integrator `ode15s` [30] to evolve in time. In the physically relevant parameter regimes, typical solutions exhibit rapid changes in the narrow Debye (boundary) layers which gives rise to significant stiffness in the DAE system. This difficulty is overcome by employing a non-uniform grid spacing. Here we do not employ the Scharfetter-Gummel scheme [34], that is widely used in other semiconductor applications, to solve the conservation equations. We note that the Scharfetter-Gummel scheme is specifically designed to address issues of charge carrier transport rather than to deal with the difficulties associated with accurately resolving the solution in narrow Debye layers, which is the main issue here.

In this section, the spatial derivatives in (11)-(17) are discretised using a finite element scheme with second-order local accuracy. The computational grid is comprised of $N+1$ arbitrarily positioned grid points, denoted by $x = x_i$ for $i = 0, ..., N$, which partition the domain $x \in [0, 1]$ into N subintervals. The widths of the subintervals are denoted by $\Delta_{i+1/2} = x_{i+1} - x_i$, and we also introduce N half-points denoted by $x_{i+1/2} = (x_i + x_{i+1})/2$ for $i = 0, ..., N-1$. A sketch of the grid is shown in figure 2. We employ a common approach in which the dependent variables are approximated as a linear combination of piecewise linear basis functions (aka 'hat' or 'tent' functions). For a generic dependent variable, w say, we write

$$w(x,t) = \sum_{i=0}^{i=N} w_i(t)\varphi_i(x) \quad \text{where} \quad \varphi_i(x) = \begin{cases} \dfrac{x - x_{i-1}}{x_i - x_{i-1}} & \text{if } x \in (x_{i-1}, x_i) \\ \dfrac{x_{i+1} - x}{x_{i+1} - x_i} & \text{if } x \in (x_i, x_{i+1}) \\ 0 & \text{if } x \notin (x_{i-1}, x_{i+1}) \end{cases} \tag{19}$$

in which $\varphi_i(x)$ are referred to as the basis functions.

On eliminating the anion vacancy flux, F^P, and the electron and hole currents, j^n and j^p, from (11)-(13) we derive three equations of the form

$$\alpha \frac{\partial w}{\partial t} = \beta \frac{\partial}{\partial x}\left(\frac{\partial w}{\partial x} \pm w \frac{\partial \phi}{\partial x}\right) + S(x, v, w), \tag{20}$$

in which α and β are constants and the source term S is a function of x, w and another generic dependent variable denoted by v. Eliminating the electric field, E, between equations (14) leads to

$$\frac{\partial^2 \phi}{\partial x^2} = \frac{1}{\lambda^2}\left(1 - P - \delta\left(p - n\right)\right). \tag{21}$$

The spatially discretised equations are derived by multiplying both (20) and (21) through by each of the test functions $\varphi_j(x)$ (for $j = 0, ..., N$), integrating over the domain $x \in (0, 1)$ (using integration by parts where appropriate) and substituting the form (19) for each of the dependent variables. On doing so we arrive at

$$\begin{aligned}\alpha \sum_{i=0}^{i=N} \frac{\mathrm{d}w_i}{\mathrm{d}t} \int_0^1 \varphi_i \varphi_j \,\mathrm{d}x = \beta \left(\frac{\partial w}{\partial x} \pm w \frac{\partial \phi}{\partial x}\right) \varphi_j \Big|_{x=0}^{x=1} \\ -\beta \left(\sum_{i=0}^{i=N} w_i \int_0^1 \varphi_i' \varphi_j' \,\mathrm{d}x \pm \sum_{i=0}^{i=N} \sum_{k=0}^{k=N} w_i \phi_k \int_0^1 \varphi_i \varphi_j' \varphi_k' \,\mathrm{d}x\right) + \int_0^1 S(x, v, w) \varphi_j \,\mathrm{d}x\,,\end{aligned} \tag{22}$$

$$\frac{\partial \phi}{\partial x} \varphi_j \Big|_{x=0}^{x=1} - \sum_{i=0}^{i=N} \phi_i \int_0^1 \varphi_i' \varphi_j' \,\mathrm{d}x = \frac{1}{\lambda^2} \left(\int_0^1 \varphi_j dx - \sum_{i=0}^{i=N} (P_i + \delta(p_i - n_i)) \int_0^1 \varphi_i \varphi_j \,\mathrm{d}x\right). \tag{23}$$

In the equations above, each of the integrals containing expressions that depend solely on the basis functions and/or their derivatives can be computed exactly (the results are given in Appendix A). Likewise, terms containing quantities evaluated on the boundaries $x = 0, 1$ can be computed exactly using the boundary conditions (15)-(16), else the relevant equation is replaced by the corresponding Dirichlet condition. The one remaining term that is not so readily computed is the final integral in (22) that depends on the source terms S. For the anion vacancy conservation, $S \equiv 0$ and so this term is zero. However, for the electron and hole conservation equations, (12) and (13), the source term comprises both the generation and recombination rates, $G(x)$ and $R(n, p)$, which are usually nonlinear. Moreover, until the physical processes in PSCs are better understood, it is desirable to maintain the flexibility to quickly alter the functional forms of these terms without necessitating significant alterations to the scheme so that, e.g., trap-assisted recombination can be augmented by radiative bimolecular recombination.

In order that the integral contained in the final term of (22) can be integrated (at least approximately) regardless of the functional form of the source term, we make a further approximation. This approximation is to replace the dependent variables in the integrand by functions that are piecewise constant over each subinterval, $x \in (x_i, x_{i+1})$, and have a value equal to that of the full series (19) at the midpoint of that interval. In short, we make

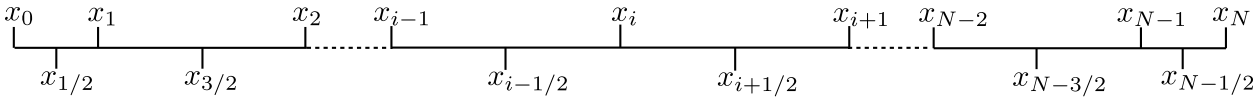

Figure 2: A schematic of the computational grid.

the additional approximation

$$\begin{aligned}\int_0^1 (G(x) - R(n,p))\varphi_j \,\mathrm{d}x \\ \approx \frac{\Delta_{j-1/2}}{2}\left(G|_{x=x_{j-1/2}} - R\left(n|_{x=x_{j-1/2}}, p|_{x=x_{j-1/2}}\right)\right) \\ + \frac{\Delta_{j+1/2}}{2}\left(G|_{x=x_{j+1/2}} - R\left(n|_{x=x_{j+1/2}}, p|_{x=x_{j+1/2}}\right)\right).\end{aligned} \tag{24}$$

The additional error incurred as a result of this approximation is comparable to the error associated with the original piecewise linear approximation for the dependent variables. Thus, even though some additional error is introduced, the scheme retains its second order local accuracy. We note that this approach to dealing with the nonlinear source terms is a special case of the method used in the work of Skeel & Berzins [35], but we emphasize that in contrast to their method, we only use this additional approximation for treatment of the source terms whilst the rest of the terms are integrated exactly. Once all the necessary integrals have been computed, the boundary conditions (15)-(16) can be imposed to form a system of DAEs which are closed by the initial conditions (17). It is this DAE system which is evolved in time using MATLAB's `ode15s`.

3.1. Spatial discretisation

In order to write down the spatially discretised system of equations in a concise form, we introduce three discrete operators: a difference operator $\mathfrak{D}_i$, an operator for evaluation of a dependent variables at a midpoint $\mathfrak{I}_i$ and a linear operator $\mathfrak{L}_i$. These act on a column vector $\mathbf{w}$ with the entries $w_i = w|_{x=x_i}$ $(i = 0, .., N)$ for a generic dependent variable w as follows:

$$\left.\frac{\partial w}{\partial x}\right|_{x=x_{i+1/2}} \approx \quad \mathfrak{D}_{i+1/2}(\mathbf{w}) = \frac{w_{i+1} - w_i}{\Delta_{i+1/2}}, \tag{25}$$

$$w|_{x=x_{i+1/2}} \approx \quad \mathfrak{I}_{i+1/2}(\mathbf{w}) = \frac{1}{2}(w_{i+1} + w_i), \tag{26}$$

$$\mathfrak{L}_i(\mathbf{w}) = \frac{1}{6}\Delta_{i+1/2}w_{i+1} + \frac{1}{3}\left(\Delta_{i+1/2} + \Delta_{i-1/2}\right)w_i + \frac{1}{6}\Delta_{i-1/2}w_{i-1}. \tag{27}$$

We introduce $\mathbf{P}(t)$, $\mathbf{\Phi}(t)$, $\mathbf{n}(t)$ and $\mathbf{p}(t)$ as column vectors of length $N+1$ whose i'th entries are the functions $P_i(t)$, $\phi_i(t)$, $n_i(t)$ and $p_i(t)$, respectively. Using this notation we obtain discretised counterparts of the electric field, anion vacancy flux and carrier currents

from (11(b)), (12(b)), (13(b)) and (14(b)) as follows,

$$E_{i+1/2} = -\mathfrak{D}_{i+1/2}(\mathbf{\Phi}), \tag{28}$$

$$F^P{}_{i+1/2} = -\left[\mathfrak{D}_{i+1/2}(\mathbf{P}) - \mathfrak{I}_{i+1/2}(\mathbf{P})E_{i+1/2}\right], \tag{29}$$

$$j^n{}_{i+1/2} = \kappa_n\left[\mathfrak{D}_{i+1/2}(\mathbf{n}) + \mathfrak{I}_{i+1/2}(\mathbf{n})E_{i+1/2}\right], \tag{30}$$

$$j^p{}_{i+1/2} = -\kappa_p\left[\mathfrak{D}_{i+1/2}(\mathbf{p}) - \mathfrak{I}_{i+1/2}(\mathbf{p})E_{i+1/2}\right]. \tag{31}$$

for $i = 0$, ..., N-1. We note that although the fluxes of the charged species and the field were eliminated in deriving the spatially discretised equations it is useful to reintroduce discrete versions of them here in the interests of brevity of notation and because it is often of interest to compute them for visualisation purposes after computations have been carried out.

The ODEs governing the evolution of the anion vacancy density, arising from (11), and ion flux boundary conditions, (15a) and (16a) are

$$\Delta_{1/2}\left[\frac{1}{3}\frac{\mathrm{d}P_0}{\mathrm{d}t} + \frac{1}{6}\frac{\mathrm{d}P_1}{\mathrm{d}t}\right] = -\lambda F^P{}_{1/2} \tag{32}$$

$$\mathfrak{L}_i\left(\frac{\mathrm{d}\mathbf{P}}{\mathrm{d}t}\right) = -\lambda\left[F^P{}_{i+1/2} - F^P{}_{i-1/2}\right], \qquad \text{for } i = 1, ..., N-1, \tag{33}$$

$$\Delta_{N-1/2}\left[\frac{1}{6}\frac{\mathrm{d}P_{N-1}}{\mathrm{d}t} + \frac{1}{3}\frac{\mathrm{d}P_N}{\mathrm{d}t}\right] = \lambda F^P{}_{N-1/2}. \tag{34}$$

The algebraic equations for the potential resulting from discretisation of (14) and the boundary conditions (15b) and (16b) are

$$0 = \phi_0 - \frac{\Phi - \Phi_{bi}}{2}, \tag{35}$$

$$0 = \lambda^2\left[E_{i+1/2} - E_{i-1/2}\right] - \mathfrak{L}_i(\mathbf{P}) + \frac{1}{2}\left[\Delta_{i+1/2} + \Delta_{i-1/2}\right] - \delta\left[\mathfrak{L}_i(\mathbf{p}) - \mathfrak{L}_i(\mathbf{n})\right] \tag{36}$$

$$\text{for } i = 1, ..., N-1,$$

$$0 = \phi_N + \frac{\Phi - \Phi_{bi}}{2}. \tag{37}$$

The ODEs for the electron and hole continuity equations, arising from (12) and (13), and the remaining boundary conditions are

$$0 = n_0 - \bar{n}, \tag{38}$$

$$\nu\mathfrak{L}_i\left(\frac{\mathrm{d}\mathbf{n}}{\mathrm{d}t}\right) = j^n{}_{i+1/2} - j^n{}_{i-1/2} + \frac{\Delta_{i+1/2}}{2}\left[G_{i+1/2} - R_{i+1/2}\right] + \frac{\Delta_{i-1/2}}{2}\left[G_{i-1/2} - R_{i-1/2}\right], \qquad \text{for } i = 1, ..., N-1, \tag{39}$$

$$\nu\Delta_{N-1/2}\left[\frac{1}{6}\frac{\mathrm{d}n_{N-1}}{\mathrm{d}t} + \frac{1}{3}\frac{\mathrm{d}n_N}{\mathrm{d}t}\right] = -j^n{}_{N-1/2} + \frac{\Delta_{N-1/2}}{2}\left[G_{N-1/2} - R_{N-1/2}\right] - R_r(n_N), \tag{40}$$

$$\nu\Delta_{1/2}\left[\frac{1}{3}\frac{\mathrm{d}p_0}{\mathrm{d}t}+\frac{1}{6}\frac{\mathrm{d}p_1}{\mathrm{d}t}\right]=-{j^p}_{1/2}+\frac{\Delta_{1/2}}{2}\left[G_{1/2}-R_{1/2}\right]-R_l(p_0), \tag{41}$$

$$\nu\mathfrak{L}_i\left(\frac{\mathrm{d}\mathbf{p}}{\mathrm{d}t}\right)=-\left[{j^p}_{i+1/2}-{j^p}_{i-1/2}\right]+\frac{\Delta_{i+1/2}}{2}\left[G_{i+1/2}-R_{i+1/2}\right] + \frac{\Delta_{i-1/2}}{2}\left[G_{i-1/2}-R_{i-1/2}\right], \qquad \text{for } i=1,...,N-1, \tag{42}$$

$$0=p_N-\bar{p}. \tag{43}$$

in which we have used the shorthand $G_{i+1/2}=G(\mathfrak{I}_{i+1/2}(\mathbf{x}))$ (in which $\mathbf{x}$ is a column vector of the values x_i, $i=0,...,N$) and $R_{i+1/2}=R(\mathfrak{I}_{i+1/2}(\mathbf{n}),\mathfrak{I}_{i+1/2}(\mathbf{p}))$.

3.2. Implementation

The system of DAEs formulated above is evolved forward in time using MATLAB's `ode15s` [36, 37] which is based on numerical differentiation formulae (of orders 1–5) or backward differentiation formulae [38] whose step size and order are automatically varied to ensure that the specified error tolerances are met. In order to minimise computational cost, by minimising the size of the system, we eliminate superfluous variables, namely F^P, j^n, j^p and E, and assemble the remaining $4N+4$ unknown functions of time into one column vector $\mathbf{u}(t)$ as follows:

$$\mathbf{u}(t)=\left[P_0,\cdots,P_N,\phi_0,\cdots,\phi_N,n_0,\cdots,n_N,p_0,\cdots,p_N\right]^{\mathrm{T}}, \tag{44}$$

$$\text{or equivalently,}\quad \mathbf{u}(t)=\left[\mathbf{P}(t)^{\mathrm{T}}\ \mathbf{\Phi}(t)^{\mathrm{T}}\ \mathbf{n}(t)^{\mathrm{T}}\ \mathbf{p}(t)^{\mathrm{T}}\right]^{\mathrm{T}}, \tag{45}$$

where a superscript T denotes a transpose. The problem to be solved can now be written in the form

$$\mathbf{M}\frac{\mathrm{d}\mathbf{u}}{\mathrm{d}t}=\mathbf{f}(\mathbf{u})\quad\text{with}\quad\mathbf{u}|_{t=0}=\mathbf{u}_0, \tag{46}$$

where $\mathbf{f}(\mathbf{u})$ is a nonlinear vector function of length $4N+4$ whose entries are the right-hand sides of (32)-(43). The matrix $\mathbf{M}$ is a $(4N+4)\times(4N+4)$ diagonal mass matrix whose entries are the coefficients of the time derivative terms in the equations (32)-(43), see figure 3. Since the governing equations for the values of ϕ_i, (35)-(37), and the discrete boundary conditions (38) and (43) contain no temporal derivatives the corresponding entries on the diagonal of $\mathbf{M}$ are zero and hence the mass matrix is singular. It is this feature of the system that renders the problem a system of DAEs and motivates our choice of solver, namely `ode15s`, which is one of relatively few solvers that can handle problems of this type. Moreover, it offers an adaptive timestep which is able to deal with the numerical stiffness resulting from the disparity in timescales between the electronic and ionic motion.

The `ode15s` time step requires numerical approximation of the Jacobian of $\mathbf{f}$. However, it is clear from the structure of the discrete system that many entries in the Jacobian are zero. A heavy reduction in computational effort (around $0.005N^{3/2}$ in the convergence test case described in §5.1) can be achieved by exploiting the `jpattern` option which allows the user to 'flag' only a subset of the entries in the Jacobian matrix that need to be numerically approximated (those that are not flagged are assumed to be zero) at each time step, see figure 3.

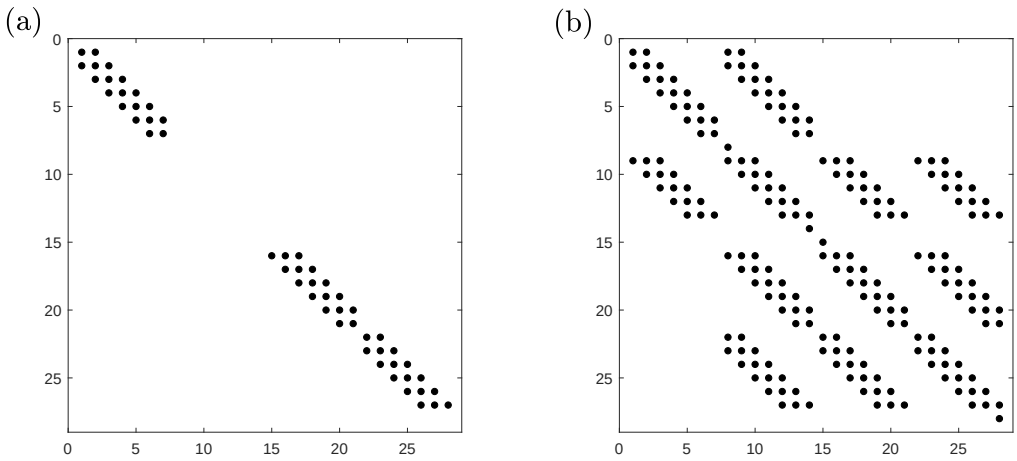

Figure 3: Plots to show the positions of the nonzero entries (black dots) in the mass matrix $\mathbf{M}$, panel (a), and the Jacobian matrix of $\mathbf{f}$, panel (b), for the finite element scheme in the case $N = 6$.

4. Finite difference scheme

In this section we outline an alternative numerical scheme for solving the model (11)-(17), in which spatial derivatives are discretised using second order accurate finite differences on a 'staggered grid'. The resulting DAEs are again evolved forward in time using MATLAB's `ode15s`. The numerical stiffness arising from narrow Debye layers is tackled by (i) employing a non-uniform grid spacing, and (ii) using Advanpix's Multiprecision Computing Toolbox [31] to overload MATLAB's native commands with arbitrary-precision counterparts, thereby retaining good accuracy despite the large condition numbers of the underlying matrices.

We retain the computational grid, including the definition of the subinterval width and half points, defined at the beginning of §3. The anion vacancy profiles are determined subject to the Neumann conditions (15a) and (16a) which require zero flux of ions at each boundary. Thus, it is natural to compute the ion vacancy flux at the grid points and the ion vacancy density at the half points. Not only does this allow (15a) and (16a) to be imposed straightforwardly, it also ensures that the property of global conservation of anion vacancies is inherited by the discrete system[1]. The equation determining the electric potential is to be solved subject to the Dirichlet conditions (15b) and (16b) which motivates tracking the potential at the grid points and the electric field at the half points. Since the governing equations for electrons (holes) are solved subject to one Dirichlet and one Neumann condition, namely (15c) and (16d) ((15d) and (16c)), it is not obvious whether it is better to define the concentration or the flux on the grid points. Here, we elect to track the concentration on the grid points and the fluxes on the half-points so that evaluating the electron and hole contributions to the charge density on the right-hand side of (14a) can

[1]Global conservation of anion vacancy concentrations in the discrete system, up to second order, is reflected in the property that $d/dt\left(\sum_{i=0}^{N-1} P_{i+1/2}\right) = 0$, see equation (58).

be accomplished without interpolation, thereby avoiding additional errors. In summary we introduce discretised variables defined by

$$P_{i+1/2} = P|_{x=x_{i+1/2}}, \qquad {F^P}_i = F^P|_{x=x_i}, \tag{47}$$

$$\phi_i = \phi|_{x=x_i}, \qquad E_{i+1/2} = E|_{x=x_{i+1/2}}, \tag{48}$$

$$n_i = n|_{x=x_i}, \qquad {j^n}_{i+1/2} = j^n|_{x=x_{i+1/2}}, \tag{49}$$

$$p_i = p|_{x=x_i}, \qquad {j^p}_{i+1/2} = j^p|_{x=x_{i+1/2}}. \tag{50}$$

Note that this means that, in this section, $\mathbf{P}$ denotes a column vector of length N (rather than $N+1$ as in §3) that comprises the entries $P_{i+1/2}$, $i = 0, ..., N-1$. We also introduce three further column vectors, also of length N, namely $\mathbf{E}$, $\mathbf{j^n}$ and $\mathbf{j^p}$ as well as one column vector of length $N+1$ namely $\mathbf{F^P}$. These have entries $E_{i+1/2}(t)$, ${j^n}_{i+1/2}(t)$, ${j^n}_{i+1/2}(t)$ for $i = 0, ..., N-1$ and ${F^P}_{i+1/2}(t)$ for $i = 0, ..., N$ respectively.

4.1. Spatial discretisation

Spatial discretisation is carried out using the discrete operators $\mathfrak{D}_{i+1/2}$ and $\mathfrak{I}_{i+1/2}$ defined in (25) and (26). We also introduce $\mathfrak{D}_i$ which approximates the first derivative at at a grid point in terms of of data at adjacent half points, and $\mathfrak{I}_i$ which linearly interpolates data at adjacent half points to return an approximation of a quantity at a grid point. These are defined as follows:

$$\left.\frac{\partial w}{\partial x}\right|_{x=x_i} \approx \quad \mathfrak{D}_i(\mathbf{w}) = \frac{w_{i+1/2} - w_{i-1/2}}{x_{i+1/2} - x_{i-1/2}}, \tag{51}$$

$$w|_{x=x_i} \approx \quad \mathfrak{I}_i(\mathbf{w}) = \frac{w_{i+1/2}(x_i - x_{i-1}) + w_{i-1/2}(x_{i+1} - x_i)}{x_{i+1} - x_{i-1}}. \tag{52}$$

A standard error analysis indicates that these both have second order local accuracy.

The discrete operators defined by (25), (26), (51) and (52) can be used to approximate the electric field, and electron and hole currents at the half-points. The discretised versions of equations (14b), (12b) and (13b) are

$$E_{i+1/2} = -\mathfrak{D}_{i+1/2}(\mathbf{\Phi}), \tag{53}$$

$${j^n}_{i+1/2} = \kappa_n \left[\mathfrak{D}_{i+1/2}(\mathbf{n}) + \mathfrak{I}_{i+1/2}(\mathbf{n})E_{i+1/2}\right], \tag{54}$$

$${j^p}_{i+1/2} = -\kappa_p \left[\mathfrak{D}_{i+1/2}(\mathbf{p}) - \mathfrak{I}_{i+1/2}(\mathbf{p})E_{i+1/2}\right], \tag{55}$$

$$\text{for} \quad i = 0, ..., N-1.$$

The anion vacancy flux can then be computed on both the internal and boundary grid points by discretising equation (11b) and its boundary conditions (15a) and (16a). We have

$${F^P}_0 = {F^P}_N = 0, \tag{56}$$

$${F^P}_i = -\mathfrak{D}_i(\mathbf{P}) - \mathfrak{I}_i(\mathbf{P})\mathfrak{I}_i(\mathbf{E}), \quad \text{for } i = 1, .., N-1. \tag{57}$$

The ODEs governing the evolution of the anion vacancy density, arising from (11a), are

$$\frac{\mathrm{d}P_{i+1/2}}{\mathrm{d}t} = -\lambda \mathfrak{D}_{i+1/2}(\mathbf{F}^{\mathbf{P}}), \quad \text{for} \quad i = 0, ..., N-1. \tag{58}$$

The algebraic equations for the potential resulting from discretisation of (14a) and the boundary conditions (15b) and (16b) are

$$\phi_0 - \frac{\Phi - \Phi_{bi}}{2} = 0, \tag{59}$$

$$\lambda^2 \mathfrak{D}_i(\mathbf{E}) + 1 - \mathfrak{I}_i(\mathbf{P}) + \delta(n_i - p_i) = 0, \quad \text{for } i = 1, .., N-1, \tag{60}$$

$$\phi_N + \frac{\Phi - \Phi_{bi}}{2} = 0. \tag{61}$$

It is straightforward to discretise (12) to derive a set of $N-1$ ODEs governing the evolution of the electron density on the internal grid points

$$n_0 - \bar{n} = 0, \tag{62}$$

$$\nu \frac{\mathrm{d}n_i}{\mathrm{d}t} = \mathfrak{D}_i(\mathbf{j^n}) + G(x_i) - R(n_i, p_i), \quad \text{for } i = 1, .., N-1, \tag{63}$$

$$j^n{}_{N-1/2} + \mathfrak{D}_{N-1}(\mathbf{j^n})(1 - x_{N-1/2}) + R_r(n_N) = 0. \tag{64}$$

Here the conditions (62) and (64) arise from the imposition of the Dirichlet boundary condition (15c) on $x = 0$ and the flux condition (16d) on $x = 1$, respectively. Notice that the latter is imposed by linear extrapolation of the electron current to the boundary $x = 0$. Similarly, discretisation of (13) leads to a set of $N-1$ ODEs governing the evolution of the hole density on the internal grid points

$$j^p{}_{1/2} - \mathfrak{D}_1(\mathbf{j^P})x_{1/2} + R_l(p_0) = 0, \tag{65}$$

$$\nu \frac{\mathrm{d}p_i}{\mathrm{d}t} = -\mathfrak{D}_i(\mathbf{j^P}) + G(x_i) - R(n_i, p_i), \quad \text{for } i = 1, .., N-1, \tag{66}$$

$$p_N - \bar{p} = 0. \tag{67}$$

Here the conditions (65) and (67) are derived from the flux condition (15d) on $x = 0$ and the Dirichlet boundary condition (16c), respectively. We note that the boundary conditions (64) and (65) are the only conditions that are not imposed exactly. However, the extrapolation involved only introduces second order errors, and therefore the scheme as a whole is still locally second order accurate as demonstrated by figure 5(a).

4.2. Implementation

The finite difference scheme is implemented using `ode15s` in the same way as the finite element scheme described in §3, except that in (45), $\mathbf{P}(t)$ is a vector of length N whose entries are the functions of time $P_{i+1/2}(t)$ for $i = 0, ..., N-1$. The problem to be solved can again be written in the form (46) where $\mathbf{f}(\mathbf{u})$ is now a nonlinear vector function of length

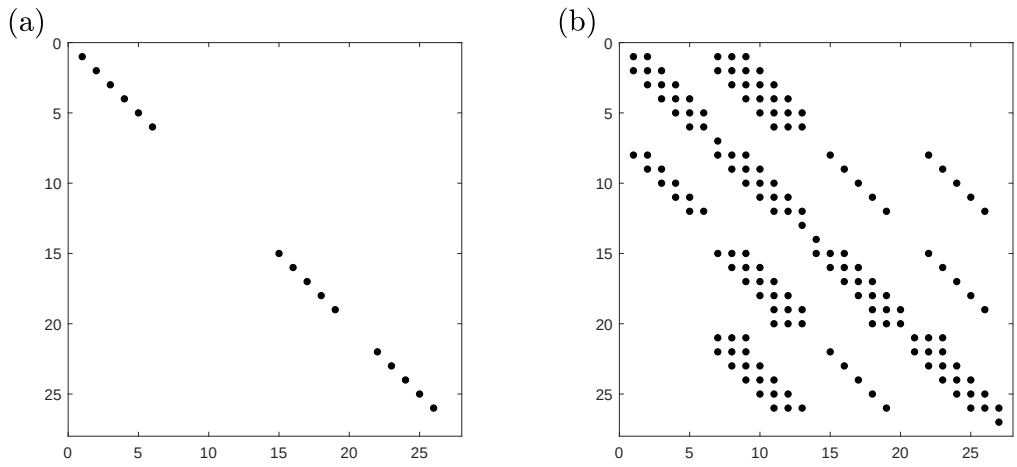

Figure 4: Plots to show the positions of the nonzero entries (black dots) in the mass matrix $\mathbf{M}$, panel (a), and the Jacobian matrix of $\mathbf{f}$, panel (b), for the finite difference scheme in the case $N = 6$.

$4N + 3$. Its first N entries are the right-hand sides of (58); the subsequent $N + 1$ entries are the right-hand sides of (59)-(61); these are followed by the $N + 1$ right-hand sides of (62)-(64); and finally the $N + 1$ right-hand sides of (65)-(67). The structure of the Jacobian is shown in figure 4. The matrix $\mathbf{M}$ is a $(4N + 3) \times (4N + 3)$ diagonal mass matrix whose entries are the coefficients of the time derivative terms in the equations (58)-(67), see figure 4.

When simulating many of the regimes of physical interest, we find that the condition number of the Jacobian is large, sometimes $O(10^{16})$ or greater, which has the potential to severely hamper the accuracy of matrix inversions performed by the solver, `ode15s`. To overcome this difficulty we make use of a third-party toolbox, Advanpix, which extends MATLAB's functionality to work with floating point numbers of higher precision. The use of quardruple precision results in a loss in the speed of computation for simple cases (those which can be computed accurately on a small number of grid points) for which runtimes, originally of a few seconds on a standard desktop computer, are typically 15-30 times longer. However, we find the higher precision offered by Advanpix's Multiprecision Computing Toolbox [31] is crucial in allowing this finite difference scheme to cope with the spatial stiffness due to narrow Debye layers.

5. Verification

Here, we demonstrate the convergence properties of our two schemes and benchmark their performance via comparison to two alternative methods. One of these alternatives has appeared in the literature [25] and makes use of MATLAB's `pdepe` solver with a piecewise constant spatial grid; the other is an adaptation of the `pdepe`-based method to the non-uniform grids introduced below in §5.2. In order to perform the benchmarking we apply the methods to a physically pertinant test case with appropraite physical parameters, as given in (18). We examine the schemes' accuracy during a transient protocol, not just near steady

state, and rate the performance in terms of numerical accuracy and computation time. We also discuss the shortcomings of previously used methods of solution including those based upon `pdepe` and the Chebfun package [39].

5.1. Choice of test case

We choose the particular scenario in which an illuminated cell is initially operating at an applied voltage equal to the built-in voltage $\Phi = \Phi_{bi} = 40$, so that the potential drop across the perovskite layer is zero. The applied voltage is then rapidly decreased to $\Phi = \Phi_{bi}/2$ so that the device is running in its power generating regime. We accomplish this by defining

$$\Phi(t) = \Phi_{bi}\left(1 - \frac{\tanh(\beta t)}{2\tanh(\beta t_{\text{end}})}\right) \quad \text{with} \quad \beta = 10^2, \quad t_{end} = 1. \tag{68}$$

Here β characterises the timescale for altering the applied voltage and t_{end} is the dimensionless time at which the simulation is terminated.

As is typical in such applications, we assume that the photo-generation rate, $G(x)$, obeys the Beer-Lambert law, which has the dimensionless form

$$G(x) = \Upsilon \exp(-\Upsilon x), \tag{69}$$

in which $1/\Upsilon$ is the dimensionless absorption length. The estimate given in Section 2 of [28] is

$$\Upsilon = 3.7. \tag{70}$$

We also choose the bulk recombination rate, $R(n,p)$, to take the form of the Shockley-Read-Hall (SRH) recombination rate (see [40] Section 4.5.5) and the interface recombination rates, $R_l(p)$ and $R_r(n)$, to both be zero, *i.e.*

$$R(n,p) = \gamma\left(\frac{np - N_i^2}{n + \epsilon p + K_3}\right), \quad R_l(p) = R_r(n) = 0, \tag{71}$$

where γ, N_i, ϵ and K_3 are dimensionless constants, defined and estimated in [28] Section 2 to be:

$$\gamma = 2.4, \qquad N_i = 8.6 \times 10^{-9}, \qquad \epsilon = 3.3 \times 10^{-3}, \qquad K_3 = 8.6 \times 10^{-9}. \tag{72}$$

All other dimensionless parameter values are also as in [28] Section 2 and listed in (18).

A simple choice of initial conditions that satisfies Poisson's equation (with $\phi|_{t=0} \equiv 0$) and six out the eight boundary conditions (those for the carrier currents are not satisfied) is

$$P_{\text{init}}(x) = 1, \quad n_{\text{init}}(x) = p_{\text{init}}(x) = \bar{p}x + \bar{n}(1-x). \tag{73}$$

In practice, the choice of initial conditions is not particularly important for the modelling of PSCs as, in any experimental procedure, it is standard practice to include a pre-conditioning step. This step involves holding the applied potential constant for a sufficiently long time such that any initial transients associated with charge carrier and ion vacancy motion decay towards zero.

5.2. Choice of spatial grid

We find that the choice of spatial grid can have a large impact on performance; this impact is shown in figure 6. In anticipation of the fact that the largest gradients in the solution appear in narrow Debye layers adjacent to the domain boundaries, we compare two spatial grids in which points are concentrated near the domain boundaries. Using this approach, we are able to achieve good resolution in the Debye layers without wasting computational effort by over-resolving in the bulk where the solution varies more slowly. The first grid is comprised of Chebyshev nodes on the interval $[0, 1]$ and defined by

$$x_i = \frac{1}{2}\left(1 + \cos\left[\pi\left(\frac{i}{N} - 1\right)\right]\right), \quad \text{for} \quad i = 0, ..., N. \tag{74}$$

We term this the *Chebyshev grid*. We define a second grid, also with points clustered toward the domain boundaries, by

$$x_i = \frac{1}{2}\left(\frac{\tanh\left[\sigma\left(\frac{2i}{N} - 1\right)\right]}{\tanh(\sigma)} + 1\right), \quad \text{for} \quad i = 0, ..., N. \tag{75}$$

We term this the *tanh grid*. Here, the parameter σ represents the degree to which points are concentrated in the Debye layers, near $x = 0$ and $x = 1$, with large values of σ giving denser clustering of points in these layers. It is possible to relate σ to the fraction X of grid points lying within a dimensionless Debye length, λ, of each domain boundary (*i.e.* in the interval $x \in [0, \lambda]$, or equivalently in the interval $x \in [1 - \lambda, 1]$) as follows

$$\lambda = \frac{1}{2}\left(\frac{\tanh\left[\sigma\left(2X - 1\right)\right]}{\tanh(\sigma)} + 1\right). \tag{76}$$

Based on our numerical tests we found that good results could be obtained by concentrating 20% (*i.e.* $X = 0.2$) of the grid points within each layer (the remaining 60% span the bulk region). This entailed taking $\sigma = 5$ for a dimensionless Debye length of $\lambda = 2.4 \times 10^{-3}$. We note that suitable values of σ depend strongly on the potential difference as well as the Debye length and so optimal values of σ may vary. In §5.3, we show the convergence of each of our schemes using the tanh grid. Then, in §5.4, we quantify the improvements made over the only previously used published method and, in §5.5, we compare all schemes considered in this work using a measure of accuracy (defined in §5.3) versus run time. Our results, shown in figure 6, demonstrate that a significant gain in performance is achieved using the tanh grid as opposed to the Chebyshev grid, regardless of the choice of scheme.

5.3. Convergence

Here we demonstrate the expected second order spatial convergence of the schemes using the test case described in §5.1. Due to the choice of non-uniform spatial grid, namely the tanh grid defined in (75) with $\sigma = 5$, we chose to monitor the values of the following five variables. This is because, independent of the number of grid points used (N+1), they are

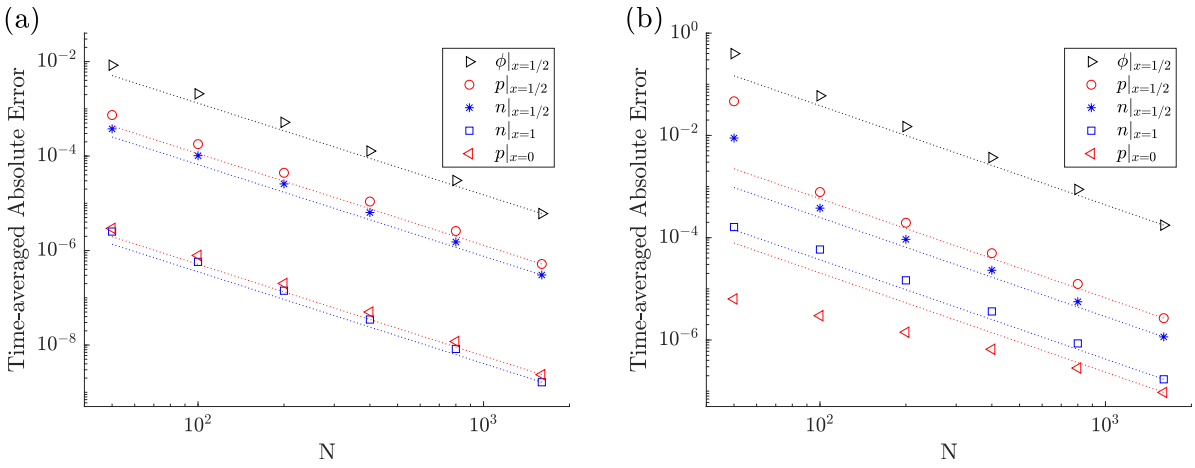

Figure 5: The pointwise convergence of (a) the finite element scheme and (b) the finite difference scheme demonstrated by plots of the time-averaged error $\bar{\mathcal{E}}$ for each of the five variables listed in (77) versus the number of subintervals, N. Markers show errors for computations with $N = 100, 200, 400, 800, 1600$ estimated against a numerical solution with $N_M = 3200$. Dotted lines show the expected second order convergence.

available immediately following the temporal integration without the need for an additional interpolation step, thereby allowing a direct interrogation of the scheme.

$$\phi|_{x=1/2}\,, \quad n|_{x=1/2}\,, \quad n|_{x=1}\,, \quad p|_{x=0}\,, \quad p|_{x=1/2}\,. \tag{77}$$

Due to the lack of exact solutions to the model, it is necessary to verify convergence by measuring the error relative to a solution computed on a highly refined grid. For some scalar quantity v (which could be any of those defined in (77)) computed using the scheme on $N+1$ grid points with N subintervals, denoted by $v^{(N)}$, we can define the absolute error at time $t = T$ of the simulation as

$$\mathcal{E}(N)|_{t=T} = \left| v^{(N)}|_{t=T} - v^{(N_M)}|_{t=T} \right| \,, \tag{78}$$

for some $N_M \gg N$. Henceforth we take $N_M = 3200$. In order to quantify the total error involved in a computation, we use this absolute error to define a time-averaged error, averaged over all but the first time point of the evolution, as follows

$$\bar{\mathcal{E}}(N) = \frac{1}{M} \sum_{i=1}^{i=M} \mathcal{E}(N)|_{t=T_i} \,, \tag{79}$$

where T_i are M equally-spaced dimensionless time points in the interval $(1/M, 1)$, i.e., $1/M$, $2/M$, ..., $(M-1)/M$, 1. This time-averaged error, for the case $M = 100$, for each of the quantities in (77) is shown in figure 5 for both the finite element and finite difference methods described in §3 and §4 respectively. We find that these errors are representative of the error at each time-step and do not grow appreciably in time. Stability of each method with respect to time is confirmed in the next section in which the relative temporal tolerance is varied, but the resulting accuracy is maintained. The computations for figure 5 were performed

with temporal integration tolerances for `ode15s` controlled using the `RelTol` and `AbsTol` settings in MATLAB; the relative tolerance was 10^{-6} and the absolute tolerance was 10^{-8}. Both sets of results demonstrate second order spatial convergence, as predicted by a naive analysis of the discrete operators (25)-(27) for the finite element scheme in §3 and (51)-(52) for the finite difference scheme in §4.

5.4. Comparison to method used by Calado et al. [25] based on MATLAB's `pdepe` *solver*

In order to benchmark our numerical schemes against an existing method, we turn to MATLAB's built-in solver `pdepe`, used by Calado *et al.* [25] to investigate a drift-diffusion model for PSCs. The `pdepe` solver is a routine which can provide numerical solution to systems of elliptic/parabolic PDEs, along with their associated boundary and initial conditions, in one spatial dimension and in time, provided that they can be cast in the 'standard form' accepted by the algorithm [35]. Temporal integration is provided by `ode15s` (like in our approaches) but for `pdepe` spatial discretisation is carried out autonomously by the solver and is based on the method presented by Skeel & Berzins [35].

Calado *et al.* [25] perform their simulations on a uniform grid with a spacing of 0.67 nm. In order to simulate on a grid with the same dimensional distance between adjacent grid points here would require $N = 900$. It is shown in the SI of [25] that appreciable differences were visible between the transient simulation results performed using a grid spacing of 0.67 nm and 0.5 nm (the smallest that was tried), indicating that numerical errors were non-negligible. It is stated in the main text that this choice was a "compromise between numerical accuracy and computation time". We find this method can be used to obtain solutions to the test case described in §5.1 (see figure 6 and associated discussion in §5.5) however our measure of the error (the sum of the time-averaged error $\bar{\mathcal{E}}$ defined in (79) for the five variables listed in (77)) is as large as 0.3 for $N = 900$. Hence this method is prone to failure when attempting to simulate longer experimental protocols such as J-V scans.

Additionally, an important disadvantage of using `pdepe` in the context of PSC simulation is that the restriction that equations must be cast in its standard form prevents the extension of the method to a three-layer model incorporating charge carrier transport in the ETL and the HTL. In particular, `pdepe` is unable to accept jump conditions posed on internal boundaries such as those occurring at the ETL/perovskite and the perovskite/HTL interfaces. Such jump conditions are used to model the discontinuities in carrier currents resulting from surface recombination. In order to circumvent this technical limitation, Calado *et al.* [25] artificially smeared the surface recombination across "diffuse" interface regions, however it is acknowledged that this approach is physically unrealistic. In contrast, the tailored numerical schemes detailed in this work can be readily extended to include more layers and incorporate any necessary type of interface condition.

5.5. Comparison between all numerical methods

Here, we compare the performance of our methods against one another as well as MATLAB's built-in solver `pdepe` using the test case described in §5.1. In figure 6 (a), the sum of the five time-averaged absolute errors (defined in §5.3) for each of the three schemes is shown versus the number of subintervals N on each of the nonlinear grids defined in §5.2. We

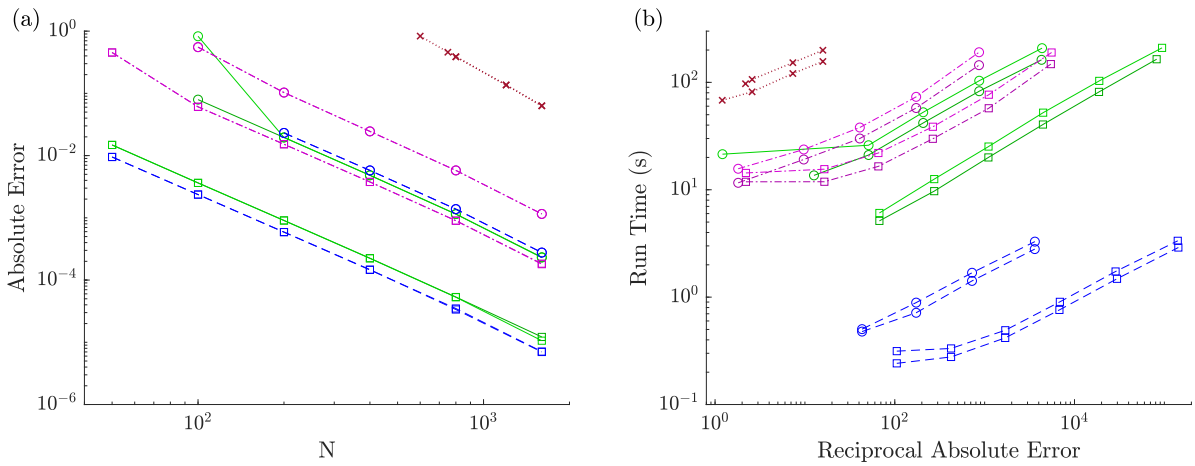

Figure 6: (a) The sum of the five time-averaged errors (as defined in (79) and plotted in figure 5) for each of the five variables listed in (77) versus the number of subintervals, N. Results are for `pdepe` (green lines), the finite difference scheme (pink dot-dashed lines) and the finite element scheme (blue dashed lines) on either the Chebyshev (circles) or tanh (squares) grid (as defined in §5.2). Red dotted lines with crosses represent results from the previously used method of `pdepe` on a uniform grid as discussed in §5.4. Lines for simulations with relative temporal tolerance of 10^{-4} and 10^{-5} are almost indistinguishable on these scales. (b) The run times for each of the simulations in (a) plotted against the reciprocal of the sum of the time-averaged errors. The higher (slower) of each pair of lines corresponds to the stricter relative temporal tolerance of 10^{-5} compared to 10^{-4}.

show results down to the lowest multiple of 50 for N for which the solver returns a solution. Second-order pointwise convergence is found in all cases, however it is notable that there is a significant decrease (improvement) in the size of the error for simulations performed on the tanh grid over those performed on the Chebyshev grid, irrespective of the method used. Figure 6 (a) also illustrates that the methods based upon the technique of finite elements, namely the scheme presented in §3 and `pdepe`, significantly outperform the finite difference scheme presented in §4, although, unlike `pdepe`, it can be readily extended to a three-layer device with interfacial recombination.

For both panels in figure 6, we apply relative temporal tolerances of 10^{-4} and 10^{-5} (applied via the `RelTol` settings in MATLAB) while the absolute tolerance is kept at 10^{-8}. In figure 6 (a), these results almost entirely overlap, indicating that the methods are stable in time. We find that all methods become unstable for relative temporal tolerances larger than 10^{-3}.

Figure 6 (b) shows the computational time required for simulation in regimes where the numerical integration was stable. We use the term "run time" to mean only the length of time taken during the simulation by the call to either `ode15s` or to `pdepe`. We choose to exclude the set-up time on grounds that this is a one-off cost that does not scale with the simulation protocol and can be avoided when running repeated simulations. Run times were recorded on a computer with a 2.40 GHz Intel processor. From the results for this test case, we conclude that computations carried out using our finite element scheme require roughly 50 times less processing time than their counterparts. These results demonstrate the increased

accuracy versus run time afforded by our finite element scheme over the finite difference scheme computed with quadruple precision and MATLAB's `pdepe`. Such improved accuracy versus run time is highly desirable and confirms that our finite element scheme provides a fast and robust tool that can enable thorough investigation of the varied behaviour of PSCs.

5.6. Comments on using the Chebfun package

We also considered schemes based on the Chebfun package available for MATLAB. We note that this has previously been used to solve PSC models, or simplifications to such models, in [22, 15, 12]. Chebfun employs spectral methods which offer high spatial accuracy when using only a relatively small number of collocation points.

Included in the Chebfun package is one of its automatic PDE solvers, `pde15s`, which (like `pdepe`) offers automatic spatial and temporal treatment of systems of elliptic/parabolic PDEs in a single spatial dimension and time. Unfortunately, it is unable to cope with the multiple sources of stiffness in this problem. We find that values of λ and/or ν below 0.25 cause the current version (at the time of writing v5.7.0) to fail. Moreover, this method is unable to deal with the nonlinearity introduced by the presence of the SRH recombination rate.

We find that it is possible to facilitate the solution of the PSC model with realistic parameter values by implementing a 'manual' timestep; we tried both straightforward backward Euler and a more complicated predictor-corrector strategy. The former approach could better cope with the extreme values of the parameters but still suffered from an inability to deal with an SRH recombination rate. The latter remedied this issue (by linearising the recombination rate), but the overheads associated with the iterative correction process mean that computations took an impractical length of time (days).

6. Comparison to asymptotic results

In this final section, we compare numerical results from our finite element scheme to the asymptotic solution presented in [28] for two physically relevant voltage protocols. To make this comparison, we use the realistic parameter estimates given in (18). The first voltage protocol is similar to that of the test case described in §5.1. The second protocol describes the measurement of a current-voltage curve. A current-voltage scan under 1 Sun illumination is the standard experimental procedure used to determine the power conversion efficiency of a solar cell. However, in the case of PSCs, such a curve often displays hysteresis as a result of ion migration which prevents accurate characterisation of their performance [14, 13]. The model and methods of solution presented in this work are intended to enable thorough investigation of the hysteresis due to ion migration during current-voltage measurements, as well as other transient protocols, in order to more thoroughly elucidate the underlying operating principles of PSCs.

Although a significant amount of progress can be made using the asymptotic method even when a nonlinear SRH recombination rate is taken, separate analytic expressions for the charge carrier concentrations can only be obtained (see [28] §3.3) when a linear, monomolecular bulk recombination rate is used. In order to compare directly to an analytic solution,

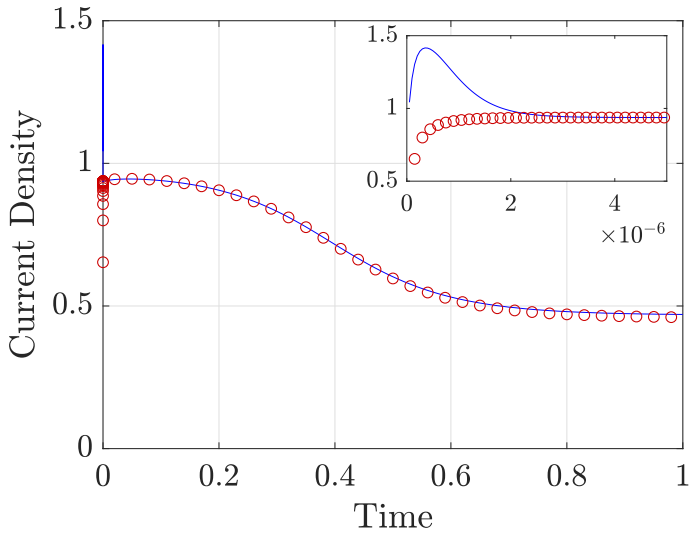

Figure 7: Current density as a function of time, in dimensionless units. Blue solid lines represent the full numerical solution and red circles represent the asymptotic result. Inset shows the extremely fast initial electronic transient which is not captured by the asymptotic solution.

that depends only on the numerical solution of a single ODE (for the Debye layer ionic charge density), we choose to compare the methods using the case where the bulk recombination, $R(n,p)$, is monomolecular (depending solely on the local hole concentration p) and the surface recombination rates, $R_l(p)$ and $R_r(n)$ are both zero, such that

$$R(n,p) = \gamma p, \quad R_l(p) = R_r(n) = 0, \tag{80}$$

where, as before, we take $\gamma = 2.4$. As noted in [28], monomolecular hole-dominated bulk recombination is the limit of the SRH recombination law, given in (71), when the electron pseudo-lifetime is much less than the hole pseudo-lifetime. This is usually a good approximation for recombination in the perovskite material methylammonium lead tri-iodide [41], however it can break down where the electron density becomes very small. Note however that the numerical schemes presented in this work are readily able to deal with nonlinear recombination rates such as the full SRH law. For further analysis of the asymptotic method and comparison to a mixed asymptotic/numeric approach that uses the full SRH law, see [28] §4.

6.1. A current decay transient

Here we simulate a cell that is preconditioned at $\Phi = \Phi_{bi} = 40$ for a sufficiently long time to eliminate transients, before undergoing a smooth but rapid decrease in applied bias from $\Phi = \Phi_{bi}$ at $t = 0$ to $\Phi = 0$ some short time later, obeying,

$$\Phi(t) = \Phi_{bi}\left(1 - \frac{\tanh(\beta t)}{\tanh(\beta t_{\text{end}})}\right) \quad \text{with} \quad \beta = 10^6, \quad t_{end} = 1. \tag{81}$$

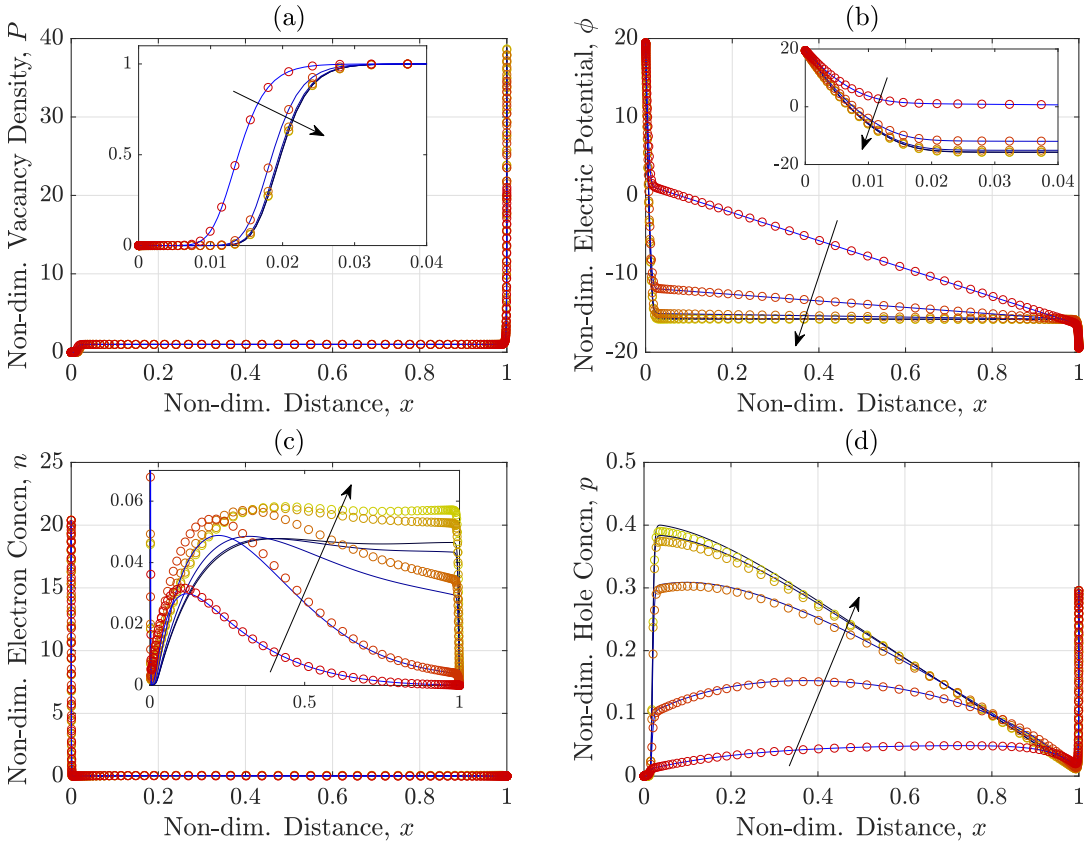

Figure 8: (a) Anion vacancy density, (b) electric potential, (c) electron concentration and (d) hole concentration profiles across the perovskite layer of a PSC at $t = 0.2, 0.4, 0.6, 0.8, 1$. Solid lines (blue to black for increasing time) represent the full numerical solutions and circles (red to yellow for increasing time) represent the uniformly-valid asymptotic expansions. Arrows indicate the direction of increasing time. Insets show magnified views of the distributions.

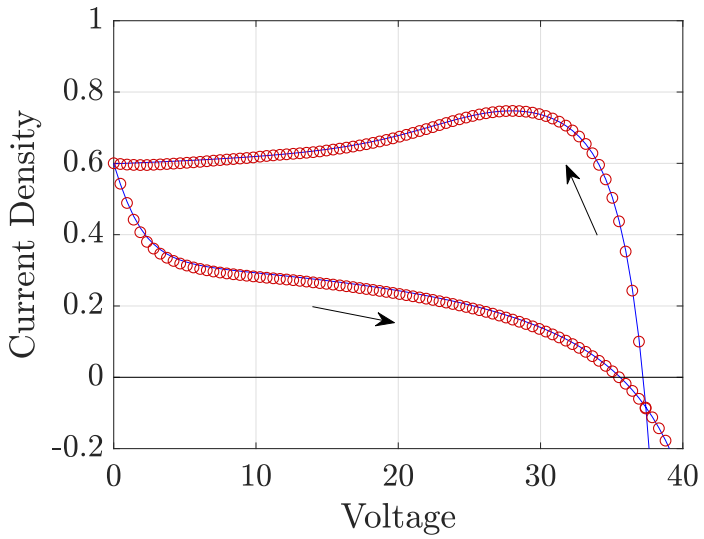

Figure 9: Current density as a function of applied voltage during the simulated 100 mV/s J-V scan. The blue line represents the full numerical solution and red circles represent the asymptotic approach. Arrows show the direction of the scan.

For this simulation, we set the number of subintervals $N = 400$ and the temporal integration tolerances $\texttt{RelTol} = 10^{-6}$ and $\texttt{AbsTol} = 10^{-8}$.

A comparison between the photocurrent calculated from the numerical solution and the asymptotic solution (as described in [28]) is made in figure 7, showing remarkable agreement between the methods for all but very small times. The deviation in very short time behaviour is shown in the inset and represents a significant advantage of the numerical method over the asymptotic method. The numerical method is able fully capture the fast timescale transients associated with charge carrier motion. In contrast, the initial rise in current density is absent from the asymptotic solution. The ability of our numerical scheme to capture fast electronic transients is key for accurate simulation of many experimental protocols (such as time-of-flight measurements and impedance spectroscopy) and therefore crucial to the systematic investigation of certain properties of PSCs.

In figure 8, we demonstrate good agreement between the numerical and asymptotic solutions, with the noticeable exception of panel (c) for the electron distribution in which the solutions vary in magnitude, but not shape. From a convergence check (increasing both spatial and temporal accuracy) and a check against an equivalent simulation using our finite difference scheme, it can be confirmed that the finite element scheme has indeed converged. The discrepancy arises from a small $O(10^{-2})$ error in the asymptotic solution to the electric potential which in turn leads to the significant error in the asymptotic solution for electron density n, that can be seen panel (c).

6.2. A current-voltage curve

Measurements of the current generated by a solar cell in response to a backwards and forwards sweep of the applied voltage are a common way of measuring cell properties and,

in the case of PSCs, frequently result in significant sweep-rate dependent *hysteresis* [14, 13]. This hysteresis is a signature of the slow timescale ion motion in the cell. The standard experimental procedure for generating such a J-V hysteresis-curve, including a preconditioning step, is simulated as follows. The cell is preconditioned by increasing the applied voltage from the built-in voltage to 1.2V (corresponding to $\Phi \approx 46.7$) over 5 seconds and held there for a further 5 seconds. Then the voltage is scanned smoothly from forward bias ($\Phi_{ap} > \Phi_{bi}$) to short circuit ($\Phi_{ap} = 0$) and back at a scan rate equivalent to 100 mV/s (corresponding to a rate of ≈ 7.1 in dimensionless units). This simulation was completed in approximately 6 seconds using our finite element scheme with $N = 400$ and `RelTol` = `AbsTol` = 10^{-8}. The resulting J-V curve is compared to the corresponding asymptotic solution from [28] in figure 9. Once again excellent agreement between the two approaches is observed.

7. Conclusions

We have presented two numerical schemes, one based on finite elements and the other based on finite differences, for solving a PDE drift-diffusion model for ion vacancy and charge carrier transport in a planar perovskite solar cell (PSC). Both approaches use the method of lines to reduce the PDEs to a (large) system of ordinary differential-algebraic equations (with time as the independent variable) which is then evolved using the MATLAB routine `ode15s` [30]. Even though the two methods are both capable of providing accurate solutions to the model in appropriate parameter regimes and use the same tool for temporal integration, the differences in their underlying spatial discretisations lead to some significant differences in their performance.

For realistic parameter values and in appropriate operating regimes, the model exhibits significant stiffness owing to (i) small Debye lengths, (ii) large potential differences across the device (giving rise to large and rapid changes in solution across the narrow Debye layers), and (iii) vastly different timescales for the transport of ion vacancies and electronic charge carriers. Both the finite element and finite difference schemes robustly cope with these difficulties by (a) utilising non-uniform meshes to selectively concentrate grids points in the Debye layers in order to maintain accuracy without prohibitive computational cost, and (b) using an adaptive timestep. Notably, computation in the relevant regime is not possible in a previously-used alternative, Chebfun, whose current version fails when realistic parameter values are taken. The finite element approach distinguishes itself as the most apt when the speed of the two methods are benchmarked. We have shown that the finite element scheme not only outperforms the finite difference method, but also another well-known alternative in MATLAB's `pdepe`, taking around 50 times less computational effort (than either of the others) to achieve a given number of digits accuracy. This makes our finite element scheme the fastest published method that is robust enough to furnish numerical solutions to a realistic charge transport model for a metal halide PSC.

We have demonstrated that our finite element method is capable of simulating a typical experimental protocol, a current-voltage sweep, in only a few seconds on a standard desktop computer. This tool therefore opens up the possibility to garner a deeper understanding of the principles that underpin the operation of PSCs, and in doing so effectively guide their

future development. Of particular interest is the identification of the dominant recombination pathway(s) in a given device architecture [42, 43, 44]. Such identification is useful for informing strategies for designing architectures that minimise the losses associated with recombination. The numerical tools described here have the potential to improve the design of cells not only by improving their power conversion efficiency but also by mitigating the build up of ions in locations that decrease a cell's usable lifetime. Degradation pathways enabled by ion vacancy motion have been identified in [45, 46]. In addition, there is increasing evidence to suggest that the motion of ions may be a factor in determining the long-term stability of PSCs [16]. Crucially, our method allows one to vary each device parameter independently (something that can often not be done by experiment) and identify its role in controlling device performance.

Acknowledgements. NEC is supported by an EPSRC funded studentship from the CDT in New and Sustainable Photovoltaics, reference EP/L01551X/1. All authors are also grateful to B. Protas, A. B. Walker, J. M. Cave and S. E. J. O'Kane for numerous insightful discussions that led to substantial improvements in the work.

[1] J.-P. Correa-Baena, A. Abate, M. Saliba, W. Tress, T. Jesper Jacobsson, M. Grätzel, A. Hagfeldt, The rapid evolution of highly efficient perovskite solar cells, Energy Environ. Sci. 10 (3) (2017) 710–727. doi:10.1039/C6EE03397K.

[2] M. Stolterfoht, C. M. Wolff, Y. Amir, A. Paulke, L. P. Toro, P. Caprioglio, D. Neher, Approaching the fill factor Shockley-Queisser limit in stable, dopant-free triple cation perovskite solar cells, Energy Environ. Sci. 10 (2017) 1530–1539. doi:10.1039/c7ee00899f.

[3] T. Miyasaka, Perovskite photovoltaics: Rare functions of organo lead halide in solar cells and optoelectronic devices, Chem. Lett. 44 (6) (2015) 720–729. doi:10.1246/cl.150175.

[4] G. Niu, X. Guo, L. Wang, Review of recent progress in chemical stability of perovskite solar cells, J. Mater. Chem. A 3 (2015) 8970. doi:10.1039/c4ta04994b.

[5] N.-G. Park, Organometal perovskite light absorbers toward a 20% efficiency low-cost solid-state mesoscopic solar cell, J. Phys. Chem. Lett. 4 (15) (2013) 2423–2429. doi:10.1021/jz400892a.

[6] S. D. Stranks, H. J. Snaith, Metal-halide perovskites for photovoltaic and light-emitting devices, Nat. Nanotechnol. 10 (5) (2015) 391–402. doi:10.1038/nnano.2015.90.

[7] T. C. Sum, S. Chen, G. Xing, X. Liu, B. Wu, Energetics and dynamics in organic-inorganic halide perovskite photovoltaics and light emitters., Nanotechnology 26 (34) (2015) 342001. doi:10.1088/0957-4484/26/34/342001.

[8] J. T. Jacobsson, J. P. Correa Baena, M. Pazoki, M. Saliba, K. Schenk, M. Grätzel, A. Hagfeldt, Exploration of the compositional space for mixed lead halogen perovskites for high efficiency solar cells, Energy Environ. Sci. 9 (2016) 1706–1724. doi:10.1039/C6EE00030D.

[9] N. Pellet, P. Gao, G. Gregori, T. Y. Yang, M. K. Nazeeruddin, J. Maier, M. Grätzel, Mixed-organic-cation perovskite photovoltaics for enhanced solar-light harvesting, Angew. Chem. Int. Ed. 53 (12) (2014) 3151–3157. doi:10.1002/anie.201309361.

[10] M. Saliba, T. Matsui, J.-Y. Seo, K. Domanski, J.-P. Correa-Baena, M. K. Nazeeruddin, S. M. Zakeeruddin, W. Tress, A. Abate, A. Hagfeldt, M. Grätzel, Cesium-containing triple cation perovskite solar cells: improved stability, reproducibility and high efficiency, Energy Environ. Sci. 9 (6) (2016) 1989–1997. doi:10.1039/C5EE03874J.

[11] I. B. Koutselas, L. Ducasse, G. C. Papavassiliou, Electronic properties of three- and low-dimensional semiconducting materials with Pb halide and Sn halide units, J. Phys.: Condens. Matter 8 (9) (1996) 1217–1227. doi:10.1088/0953-8984/8/9/012.

[12] S. E. J. O'Kane, G. Richardson, A. Pockett, R. G. Niemann, J. M. Cave, N. Sakai, G. E. Eperon, H. J. Snaith, J. M. Foster, P. J. Cameron, A. B. Walker, Measurement and modelling of dark current decay transients in perovskite solar cells, J. Mater. Chem. C 5 (2017) 452–462. doi:10.1039/C6TC04964H.

[13] E. Unger, E. Hoke, C. Bailie, W. Nguyen, A. Bowring, T. Heumüller, M. Christoforo, M. McGehee, Hysteresis and transient behavior in current–voltage measurements of hybrid-perovskite absorber solar cells, Energy Environ. Sci. 7 (11) (2014) 3690–3698.

[14] H. J. Snaith, A. Abate, J. M. Ball, G. E. Eperon, T. C. Leijtens, N. K. Noel, S. D. Stranks, J. T.-W. Wang, K. Wojciechowski, W. Zhang, Anomalous hysteresis in perovskite solar cells, J. Phys. Chem. Lett. 5 (9) (2014) 1511–1515. doi:10.1021/jz500113x.

[15] G. Richardson, S. E. J. O'Kane, R. G. Niemann, T. A. Peltola, J. M. Foster, P. J. Cameron, A. B. Walker, Can slow-moving ions explain hysteresis in the current-voltage curves of perovskite solar cells?, Energy Environ. Sci. 9 (2016) 1476–1485. doi:10.1039/C5EE02740C.

[16] K. Domanski, B. Roose, T. Matsui, M. Saliba, S.-H. Turren-Cruz, J.-P. Correa-Baena, C. Roldán Carmona, G. Richardson, J. M. Foster, F. De Angelis, J. M. Ball, A. Petrozza, N. Mine, M. K. Nazeeruddin, W. Tress, M. Grätzel, U. Steiner, A. Hagfeldt, A. Abate, Migration of cations induces reversible performance losses over day/night cycling in perovskite solar cells, Energy Environ. Sci. 10 (2017) 604–613. doi:10.1039/C6EE03352K.

[17] C. Eames, J. M. Frost, P. R. F. Barnes, B. C. O'Regan, A. Walsh, M. S. Islam, Ionic transport in hybrid lead iodide perovskite solar cells, Nat. Commun. 6 (2015) 7497. doi:10.1038/ncomms8497.

[18] L. Cojocaru, S. Uchida, P. V. Jayaweera, S. Kaneko, J. Nakazaki, T. Kubo, H. Segawa, Origin of the hysteresis in I–V curves for planar structure perovskite solar cells rationalized with a surface boundary-induced capacitance model, Chem. Lett. 44 (12) (2015) 1750–1752.

[19] G. A. Buxton, N. Clarke, Predicting structure and property relations in polymeric photovoltaic devices, Phys. Rev. B 74 (8) (2006) 085207.

[20] J. M. Foster, J. Kirkpatrick, G. Richardson, Asymptotic and numerical prediction of current-voltage curves for an organic bilayer solar cell under varying illumination and comparison to the Shockley equivalent circuit, J. Appl. Phys. 114 (10) (2013) 104501. doi:10.1063/1.4820567.

[21] G. Richardson, C. Please, V. Styles, Derivation and solution of effective medium equations for bulk heterojunction organic solar cells, Eur. J. Appl. Math. (2017) 1–42.

[22] J. M. Foster, H. J. Snaith, T. C. Leijtens, G. Richardson, A Model for the Operation of Perovskite Based Hybrid Solar Cells: Formulation, Analysis, and Comparison to Experiment, SIAM J. Appl. Math. 74 (6) (2014) 1935–1966. doi:10.1137/130934258.

[23] X. Li, N. P. Hylton, V. Giannini, K.-H. Lee, N. J. Ekins-Daukes, S. A. Maier, Multidimensional modeling of solar cells with electromagnetic and carrier transport calculations, Prog. Photovoltaics Res. Appl. 21 (1) (2013) 109–120.

[24] S. van Reenen, M. Kemerink, H. J. Snaith, Modeling anomalous hysteresis in perovskite solar cells, J. Phys. Chem. Lett. 6 (19) (2015) 3808–3814. doi:10.1021/acs.jpclett.5b01645.

[25] P. Calado, A. M. Telford, D. Bryant, X. Li, J. Nelson, B. C. O'Regan, P. R. Barnes, Evidence for ion migration in hybrid perovskite solar cells with minimal hysteresis, Nat. Commun. 7 (2016) 13831. doi:10.1038/ncomms13831.

[26] D. Jacobs, Y. Wu, H. Shen, C. Barugkin, F. Beck, T. White, K. Weber, K. Catchpole, Hysteresis phenomena in perovskite solar cells: the many and varied effects of ionic accumulation, Phys. Chem. Chem. Phys. 19 (2017) 3094–3103. doi:10.1039/C6CP06989D.

[27] R. Gottesman, P. Lopez-varo, L. Gouda, J. A. Jimenez-Tejada, J. Hu, S. Tirosh, A. Zaban, J. Bisquert, Dynamic phenomena at perovskite / electron- selective contact interface as interpreted from photovoltage decays, Chem 1 (5) (2016) 776–789. doi:10.1016/j.chempr.2016.10.002.

[28] N. E. Courtier, J. M. Foster, S. E. J. O'Kane, A. B. Walker, G. Richardson, Systematic derivation of a surface polarization model for planar perovskite solar cells, arXiv:1708.09210.

[29] A. Walsh, D. O. Scanlon, S. Chen, X. G. Gong, S. H. Wei, Self-regulation mechanism for charged point defects in hybrid halide perovskites, Angew. Chem. Int. Ed. 54 (6) (2015) 1791–1794. doi:10.1002/anie.201409740.

[30] MATLAB version 9.3.0.713579 (R2017b) (2017).

[31] Advanpix Multiprecision Computing Toolbox for MATLAB 4.3.2.12144 (2017).

[32] G. Richardson, A multiscale approach to modelling electrochemical processes occurring across the cell membrane with application to transmission of action potentials, Math. Med. Biol. 26 (3) (2009) 201–224.

[33] S. George, J. M. Foster, G. Richardson, Modelling in vivo action potential propagation along a giant axon, J. Math. Biol. 70 (1-2) (2015) 237–263. doi:10.1007/s00285-013-0751-x.

[34] D. L. Scharfetter, H. K. Gummel, Large-signal analysis of a silicon read diode oscillator, IEEE Trans. Electron Devices 16(1) (1969) 64–77.

[35] R. D. Skeel, M. Berzins, A method for the spatial discretization of parabolic equations in one space variable, SIAM journal on scientific and statistical computing 11 (1) (1990) 1–32.

[36] L. F. Shampine, M. W. Reichelt, The MATLAB ODE suite, SIAM J Sci. Comput. 18 (1) (1997) 1–22.

[37] L. F. Shampine, M. W. Reichelt, J. A. Kierzenka, Solving index-1 DAEs in MATLAB and Simulink, SIAM Rev. 41 (3) (1999) 538–552.

[38] C. W. Gear, Numerical Initial Value Problems in Ordinary Differential Equations, Prentice Hall PTR, Upper Saddle River, NJ, USA, 1971.

[39] T. A. Driscoll, N. Hale, L. N. Trefethen, Chebfun guide (2014).

[40] J. Nelson, The Physics of Solar Cells, Imperial College Press, London, UK, 2003.

[41] S. D. Stranks, V. M. Burlakov, T. Leijtens, J. M. Ball, A. Goriely, H. J. Snaith, Recombination kinetics in organic-inorganic perovskites: excitons, free charge, and subgap states, Phys. Rev. Appl 2 (3) (2014) 034007.

[42] C. M. Wolff, F. Zu, A. Paulke, L. P. Toro, N. Koch, D. Neher, Reduced interface-mediated recombination for high open-circuit voltages in $CH_3NH_3PbI_3$ solar cells, Advanced Materials 29 (2017) 1700159. doi:10.1002/adma.201700159.

[43] J.-P. Correa-Baena, W. Tress, K. Domanski, E. H. Anaraki, S.-H. Turren-Cruz, B. Roose, P. P. Boix, M. Grätzel, M. Saliba, A. Abate, A. Hagfeldt, Identifying and suppressing interfacial recombination to achieve high open-circuit voltage in perovskite solar cells, Energy & Environmental Science 10 (2017) 1207–1212. doi:10.1039/C7EE00421D.

[44] L. Contreras-Bernal, M. Salado, A. Todinova, L. Calio, S. Ahmad, J. Idígoras, J. A. Anta, Origin and whereabouts of recombination in perovskite solar cells, The Journal of Physical Chemistry C 121 (18) (2017) 9705–9713. doi:10.1021/acs.jpcc.7b01206.

[45] N. Aristidou, C. Eames, I. Sanchez-Molina, X. Bu, J. Kosco, M. Islam, S. A. Haque, Fast oxygen diffusion and iodide defects mediate oxygen-induced degradation of perovskite solar cells, Nature Communications 8 (2017) 15218. doi:10.1038/ncomms15218.

[46] J. Carrillo, A. Guerrero, S. Rahimnejad, O. Almora, I. Zarazua, E. Mas-Marza, J. Bisquert, G. Garcia-Belmonte, Ionic reactivity at contacts and aging of methylammonium lead triiodide perovskite solar cells, Advanced Energy Materials 6 (9). doi:10.1002/aenm.201502246.

Appendix A. Integrals required for the finite element discretisation

In §3 when using the finite element approach to discretise the governing system (11)-(16) in space the following results are needed:

$$\int_0^1 \varphi_i \varphi_j \,\mathrm{d}x = \begin{cases} \frac{1}{3}\left(\Delta_{j+1/2} + \Delta_{j-1/2}\right) & \text{if } i = j \text{ and } j = 1, ..., N-1 \\ \frac{1}{3}\Delta_{1/2} & \text{if } i = j \text{ and } j = 0 \\ \frac{1}{3}\Delta_{N-1/2} & \text{if } i = j \text{ and } j = N \\ \frac{1}{6}\Delta_{j+1/2} & \text{if } i = j+1 \text{ and } j = 0, ..., N-1 \\ \frac{1}{6}\Delta_{j-1/2} & \text{if } i = j-1 \text{ and } j = 1, ..., N \\ 0 & \text{otherwise} \end{cases} \tag{A.1}$$

$$\int_0^1 \varphi_i' \varphi_j' \,\mathrm{d}x = \begin{cases} \frac{1}{\Delta_{j+1/2}} + \frac{1}{\Delta_{j-1/2}} & \text{if } i = j \text{ and } j = 1, ..., N-1 \\ \frac{1}{\Delta_{1/2}} & \text{if } i = j \text{ and } j = 0 \\ \frac{1}{\Delta_{N-1/2}} & \text{if } i = j \text{ and } j = N \\ \frac{-1}{\Delta_{j+1/2}} & \text{if } i = j+1 \text{ and } j = 0, ..., N-1 \\ \frac{-1}{\Delta_{j-1/2}} & \text{if } i = j-1 \text{ and } j = 1, ..., N \\ 0 & \text{otherwise} \end{cases} \tag{A.2}$$

$$\int_0^1 \varphi_i \varphi_j' \varphi_k' \, \mathrm{d}x = \begin{cases} \dfrac{1}{2\Delta_{j+1/2}} + \dfrac{1}{2\Delta_{j-1/2}} & \text{if } i = j,\ k = j \text{ and } j = 1, ..., N-1. \\ \dfrac{1}{2\Delta_{1/2}} & \text{if } i = j,\ k = j \text{ and } j = 0 \\ \dfrac{1}{2\Delta_{N-1/2}} & \text{if } i = j,\ k = j \text{ and } j = N \\ -\dfrac{1}{2\Delta_{j+1/2}} & \text{if } i = j,\ k = j+1 \text{ and } j = 0, ..., N-1 \\ -\dfrac{1}{2\Delta_{j-1/2}} & \text{if } i = j,\ k = j-1 \text{ and } j = 1, ..., N \\ -\dfrac{1}{2\Delta_{j+1/2}} & \text{if } i = j+1,\ k = j+1 \text{ and } j = 0, ..., N-1 \\ \dfrac{1}{2\Delta_{j+1/2}} & \text{if } i = j+1,\ k = j \text{ and } j = 0, ..., N-1 \\ -\dfrac{1}{2\Delta_{j-1/2}} & \text{if } i = j-1,\ k = j-1 \text{ and } j = 1, ..., N \\ \dfrac{1}{2\Delta_{j-1/2}} & \text{if } i = j-1,\ k = j \text{ and } j = 1, ..., N \\ 0 & \text{otherwise} \end{cases} \tag{A.3}$$

$$\int_0^1 \varphi_j \, \mathrm{d}x = \begin{cases} \dfrac{1}{2}\left(\Delta_{j+1/2} + \Delta_{j-1/2}\right) & \text{if } j = 1, ..., N-1 \\ \dfrac{1}{2}\Delta_{1/2} & \text{if } j = 0 \\ \dfrac{1}{2}\Delta_{N-1/2} & \text{if } j = N \\ 0 & \text{otherwise} \end{cases} \tag{A.4}$$

where $\varphi_i(x)$ is a basis function often referred to as the 'hat' or 'tent' function and is defined in (19), a prime denotes a derivative with respect to x, and the indices $i, j, k = 0, ..., N$.